Materials Today Bio 22 (2023) 100730

Contents lists available at ScienceDirect

Materials Today Bio

journal homepage: www.journals.elsevier.com/materials-today-bio

Amyloid-like nanofibrous network confined and aligned ultrafine bimetallic nanozymes for smart antibacterial therapy

Yonghai Feng [a], Zerui Cheng [a], Anne-Kathrine Kure Larsen [b], Hui Shi [c], Tongtong Sun [a], Peng Zhang [d], Mingdong Dong [b,*], Lei Liu [a,**]

[a] Institute for Advanced Materials, School of Materials Science and Engineering, Jiangsu University, 301 Xuefu Road, Zhenjiang, 212013, China
[b] Interdisciplinary Nanoscience Center, Universitas Arhusiensis, Arhus, 8200, Denmark
[c] School of Medicine, Jiangsu University, 301 Xuefu Road, Zhenjiang, 212013, China
[d] Institute of Environmental Research at Greater Bay, Guangzhou University, 230 Waihuan West Road, Guangzhou Higher Education Mega Center, Guangzhou, 510006, China

ARTICLE INFO

Keywords:
Lysozyme assemblies
Bimetallic gold and copper nanoparticles
Nanozymes
Antibacterial
Bacterial capture

ABSTRACT

Nanozyme-based antibacterial therapy (NABT) has emerged as a promising strategy to combat bacterial antimicrobial resistance. Engineering the noble metal nanozymes with strong bacterial capture and high catalytic activity for enhanced NABT is highly anticipated but still challenged. Herein, we developed hybrid nanozymes by engineering ultrafine bimetallic Au/Cu nanoparticles confined on the lysozyme amyloid-like nanofibrous networks (LNF). The introduction of copper in the nanozymes facilitates the H_2O_2 adsorption and reduces the energy barrier for activating the H_2O_2 decomposition to form •OH, meanwhile displaying the significantly enhanced POD-like activity under NIR irradiation. Taking advantage of the inherent supramolecular networks inspired from human defensin 6-trapping bacteria mechanism, the hybrid nanozymes effectively capture the bacteria and allow the catalytic attack around the bacterial surfaces to improve the antibacterial efficiency. Finally, the as-prepared nanozymes exhibit the preeminent bactericidal efficacy against bacteria, especially for drug-resistant bacteria both in vitro and *in vivo*, and the effect on wound healing.

1. Introduction

Bacterial antimicrobial resistance (AMR) has emerged as one of the top ten public health threats, which can be dominantly attributed to the changes in bacteria with the characteristic of multidrug resistance caused by the long-term overuse or misuse of antibiotics [1], leading to the increasing difficulty in the treatment of bacterial infection. Recently, nanozyme-based antibacterial therapy (NABT) has emerged as an alternative promising strategy to combat AMR due to the broad-spectrum antibacterial activity and no-resistance effect [2–7]. Particularly, profiting from the intrinsic enzyme-mimetic activity, unique plasmonic feature, and good biocompatibility and stability, noble-metal nanoparticles (e.g., Au, Pt, Pd NPs) are burgeoning for NABT [8–15]. For instances, Au NPs immobilized on mesoporous silica can kill Gram-positive *Staphylococcus aureus* (*S. aureus*) and Gram-negative *Escherichia coli* (*E. coli*) under physiological condition based on the catalytic production of $^1O_2$, $\bullet OH^-$, and $\bullet O_2^-$ in an acidic pH [16]. Some alternative Au nanostructures, such as Au nanoplates [15], can take advantage of strong localized surface plasmon resonance (LSPR) absorption in the near infrared (NIR) region to generate a great number of hot carriers, which can burn the bacteria to death, and simultaneously the photothermal effect is able to accelerate the production of reactive oxygen species (ROS), thus synergistically enhancing the antibacterial efficacy. In this case, the development of photothermal nanozymes for antibacterial therapy has attracted great interesting [15, 17–20]. However, it is noted that the short lifetime (<200 ns) and limited diffusion distance (ca. 20 nm) of reactive oxygen species (ROS) [21], usually critically require the antibacterial nanozymes to possess strong bacterial capturing capacity, so that it can maximize the oxidative attack of ROS on the vicinal membranes of microbes. However, the insufficient bacterial capturing capacity of noble-metal nanozymes remarkably restricts the amplification of catalytic bactericidal efficiency. Although the surface modification strategy can improve the interaction between bacteria and nanozymes, it comes out at the cost of

* Corresponding author.
** Corresponding author.
E-mail addresses: dong@inano.au.dk (M. Dong), liul@ujs.edu.cn (L. Liu).

https://doi.org/10.1016/j.mtbio.2023.100730
Received 5 May 2023; Received in revised form 30 June 2023; Accepted 10 July 2023
Available online 20 July 2023

active sites blocking, especially for those highly-active ultrasmall metal nanozymes (~2 nm). Therefore, it is imperative to explore a new way to engineer smart noble metal nanozymes with strong bacterial capture and high catalytic activity for enhanced NABT.

Although some strategies have been proposed, i.e., engineering rough-surface hybrid nanozymes (defect-rich layered MoS_2 nanosheets on the surfaces of 0D Fe_3O_4 nanospheres) by virtue of the intrinsic topological interactions between bacteria and rough surface [2,22–25], and spiky noble-metal nanostructures inspired by the bacterial trapping mechanism of the pseudopodia of neutrophil in human immune system [26], which has paved the ways for the design of smart nanozymes. There is still some challenge in developing novel nanozymes. Nevertheless, either rough-surface or spiky noble-metal nanostructures such as Au nanoflowers [27], and nanostars [28] are usually large size (>100 nm), of which the atom utilization efficiency is far lower than that of ultrasmall Au NPs (~2 nm), undoubtedly decreasing the catalytic activity. Therefore, it is highly anticipated to develop an efficient approach to both improve the bacterial capturing and maintain the intrinsic high enzyme-like activity of ultrasmall noble-metal NPs.

In this work, we proposed a strategy to form hybrid nanozymes by engineering ultrasmall noble-metal NPs confined on the lysozyme amyloid-like nanofibrous networks. It is inspired from the human defensin 6 (HD6)-trapping bacteria mechanism by tangled nanofibrous networks capturing microbial pathogens to block the invasion to host cell [29], meanwhile, amyloid-like hierarchical supramolecular nanofibrous networks (HSNW) could control the growth of metal crystal to small particles [30–32], with possible high catalytic activity comparable to that of isolated metal NPs. In details, we first used the lysozyme nanofibril (LNF) as an alternative HSNW template to confine and modulate the formation and alignment of ultrafine bimetallic Au and Cu (Au_mCu_n, m and n represent the number of the mole ratio of Au/Cu, m = 1–4 and n = 1) alloyed NPs on the surfaces of LNF (LNF/Au_mCu_n HSNW). Both experimental studies and theoretical calculation reveal that the introduction of Cu species not only facilitates the H_2O_2 adsorption and reduces the energy barrier for activating the H_2O_2 decomposition, significantly enhancing the peroxidase (POD)-like activity, but also improves the NIR absorption that could accelerate the catalytic reaction rate. Taking advantage of the inherent supramolecular networks, LNF/Au_mCu_n HSNW effectively captures the bacteria and allows the catalytic attack around the bacterial surfaces. Particularly, the antibacterial performance can be significantly enhanced upon NIR irradiation due to the synergy between the enhanced •OH production and the photothermal ablation. Therefore, the LNF/Au_mCu_n HSNW exhibits the preeminent bactericidal efficacy against drug-resistant bacteria both in vitro and *in vivo*, which would play a novel nanozyme for combating AMR.

2. Experimental section/methods

2.1. Materials

Acetic acid, glycine, choline chloride, hydrochloroauric acid ($HAuCl_4{\cdot}4H_2O$), cupric chloride ($CuCl_2$), and sodium borohydride ($NaBH_4$) were purchased from Sinopharm Chemical Reagent Co., LTD. Lysozyme, 3,3′,5,5′-tetramethylbenzidine (TMB), were bought from Shanghai Aladdin Bio-Chem Technology Co., LTD.

2.2. Synthesis of lysozyme nanofibers

First, 10 mM hydrochloric acid solution and 1 mM acetic acid solution were prepared. 0.015 g of glycine and 0.1395 g of choline chloride were weighed and dissolved in 10 mL of hydrochloric acid solution and 1 mL of acetic acid solution, respectively. Then, 0.01 g of lysozyme monomer was added to the hydrochloric acid-glycine solution (4.75 mL) and the acetic acid-choline chloride solution (250 μL). The whole system was placed in an oil bath at 70 °C and stirred for 5 h. Finally, the reacted solution was washed twice by centrifugation (12,000 rpm, 20 min) and then stored at 4 °C, obtaining 10 mg mL^{-1} lysozyme nanofiber (LNF) solution.

2.3. Synthesis of LNF/Au_mCu_n nanostructures

First, $HAuCl_4$ and $CuCl_2$ solutions with concentration of 1.5 mM, respectively, were prepared. Then, 800 μL of $HAuCl_4$ and $CuCl_2$ mixed solutions in different volume proportions of 4:1, 3:1, 2:1, 1:1, respectively, were added into 800 μL of LNF solution (5 mg mL^{-1}), and incubated for more than 30 min. Subsequently, 800 μL $NaBH_4$ solution (10 mM) was added into the mixture with appropriate shaking, allowing the gas to escape. When no bubbles are generated, a bimetallic Au and Cu alloying NPs supported by LNF HSNW (*LNF/Au_mCu_n*) with different Au/Cu ratios were obtained. The monometallic LNF/Au and LNF/Cu HSNW were also prepared by following the same procedure but just with pure $HAuCl_4$ or $CuCl_2$ solutions (800 μL) as the raw materials.

2.4. Characterizations

Transition electronic microscope (TEM) images showing the morphology were captured using a JEM-2100(HR) transmission electron microscope. The crystal structures of *LNF/Au_mCu_n* nanostructures were characterized using a Bruker D8 ADVANCE X-ray diffractometer. X-ray photoelectron spectroscopy (XPS) spectra was carried out using a Thermo Fisher-Nexsa instrument. Meanwhile, the UV–visible absorbance spectra were obtained by using a UV-1601 spectrophotometer. The electron-spin-resonance (ESR) spectra were recorded using a Bruker A300-10/12 spectrometer. The Au and Cu contents were measured by the inductively coupled plasma spectrometer (ICP-MS, Agilent 7800).

2.5. Photothermal properties of LNF/Au_mCu_n nanostructures

LNF/Au_mCu_n nanostructures with different metal ratios were irradiated with an 808 nm laser (2.0 W cm^{-2}) for 600 s at room temperature. And an infrared thermal imager was used to record the temperature in real time. Pure water was irradiated in the same way as a control group. LNF/Au_mCu_n nanostructures were irradiated at 2 W cm^{-2} for 5 cycles. Each cycle consisted of a 600 s heating period and natural cooling, which was used to test the photothermal stability of LNF/Au_mCu_n nanostructures.

2.6. Peroxidase-like activity of LNF/Au_mCu_n nanostructures

Peroxidase (POD)-mimetic assays for LNF/Au_mCu_n nanozymes were performed in NaAc-HAc buffer solution (0.1 M) at pH = 5.5 with TMB as substrate. After reacting for 30 min, the UV absorption spectrum of the color reaction for each solution was recorded. All kinetic measurements were performed in a time-sweep fashion at 520 nm by a Shimadzu UV spectrophotometer. Steady-state kinetic analyses were performed at room temperature. The final concentrations of H_2O_2 and TMB were 416 μM at 5 mM, respectively, with the LNF/Au_mCu_n concentration of 8 μg mL^{-1}. For kinetic parameters, the experiments were carried out in a 2 mL NaAc-HAc buffer containing 20 μg mL^{-1} LNF/Au_mCu_n, 832 μM TMB, and a series of concentrations of H_2O_2 ranging from 0 to 150 mM, or containing 20 μg mL^{-1} LNF/Au_mCu_n, 150 mM H_2O_2 and a series of concentrations of TMB ranging from 0 to 832 μM. The molar concentration of LNF/Au_mCu_n was calculated by using the NanoSight NS300 (Malvern Instruments, Malvern, UK) nanoparticle tracking analyzer. All experiments were tested in triplicate. The Michaelis-Menten constant is calculated according to the following formula:

$$1/v = K_m/V_{max}[S]+1/V_{max}$$

where ν is the initial velocity, K_m is the Michaelis constant, [S] is the substrate concentration, and Vmax is the maximum reaction velocity.

For pH-dependent experiments, the enzyme-like activities of LNF/Au_3Cu_1 were detected in buffer solutions with different pH ranges (3.0–8.0). For temperature-dependent experiments, in buffer solutions with pH = 5.5, the enzyme-like activities of LNF/Au_3Cu_1 were measured at different temperatures of 20~55 °C.

2.7. In vitro cytotoxicity assay

The in vitro cytotoxicity of LNF/Au_3Cu_1 nanostructures was detected by CCK-8 cell viability assay kit was detected with mouse fibroblasts (L929) cells as the model cells. Briefly, L929 cells were seeded in 96-well plates at a cell density of 5×10^3 per well, and cultured in 1640 medium for 24 h. The blank group (n = 6) with only 1640 medium was defined as 0%. L929 cells treated with PBS alone (n = 6) were defined as 100%. After the cells were treated with LNF/Au_3Cu_1 (0–160 μg mL^{-1}) for 24 h, 10 μl of CCK-8 solution was added to each well and incubated at 37 °C for 4 h. Finally, the absorbance value at 450 nm was measured. Each independent experiment was tested in triplicate.

2.8. In vitro antibacterial experiments

Single colonies of Gram-negative bacteria *Escherichia coli* (*E. coli*) and Gram-positive bacteria *Staphylococcus aureus* (*S. aureus*) streaked on Luria-Bertani (LB) solid agar medium were transferred to about 20 mL of liquid LB medium at 37 °C and incubated at 160 rpm for 12 h, which was then centrifuged (4000 rpm, 1min) to collect bacteria. Bacteria were resuspended in PBS (10 mM, pH = 7.4) and diluted to an optical density of 0.1 at 600 nm (OD600 = 0.1). The antibacterial experiments were then carried out in NaAc-HAc buffer solution (0.1 M) at pH = 5.5. The bactericidal efficiency of LNF/Au_3Cu_1 nanozyme on *E. coli* and MRSA was detected by plate counting method, which were treated with seven different groups: (1) NaAc-HAc, (2) LNF/Au_3Cu_1, (3) LNF/Au_3Cu_1+H_2O_2, (4) LNF/Au_3Cu_1+NIR, (5) LNF/Au_3Cu_1+H_2O_2+NIR, (6) NIR, (7) H_2O_2. The final concentrations of LNF/Au_3Cu_1 and H_2O_2 were 80 μg mL^{-1} and 200 μM, respectively. After the mixed solutions of each group were reacted for 10 min, the solution was transferred to LB solid medium by the method of dilution plate coating for 24 h at 37 °C. All experiments were tested in triplicate.

2.9. Healing efficiency for MRSA infected mouse wound model

First, MRSA infected wound model was established on the back of ICR mice (6–8 weeks) by slashing the back of mice and injecting MRSA bacteria with concentration of 1×10^6 CFU. Then, the mice were separated into seven groups (five mice per group), treated with (1) NaAc-HAc, (2) LNF/Au_3Cu_1, (3) LNF/Au_3Cu_1+H_2O_2, (4) LNF/Au_3Cu_1+NIR, (5) LNF/Au_3Cu_1+H_2O_2+NIR, (6) NIR, (7) H_2O_2, respectively. The wounds were observed, photographed as well as Band-Aids were replaced every day. After 3 days of therapeutic process, the mice were examined and the wound tissues were collected and the numbers of bacteria in them were determined by plate count methods. Back skins were harvested on the day 14, the wound was isolated from the surrounding skin and immobilized in a 4% neutral formalin solution. The skin samples were embedded in paraffin, sectioned for HE histology and immunohistochemistry. Noted that all animal procedures were approved by Jiangsu University and carried out in accordance with the Guidelines for Care and Use of Laboratory Animals of Jiangsu University, and conformed to the Animal Ethics Committees of both Chinese legislation and the National Institutes of Health (NIH).

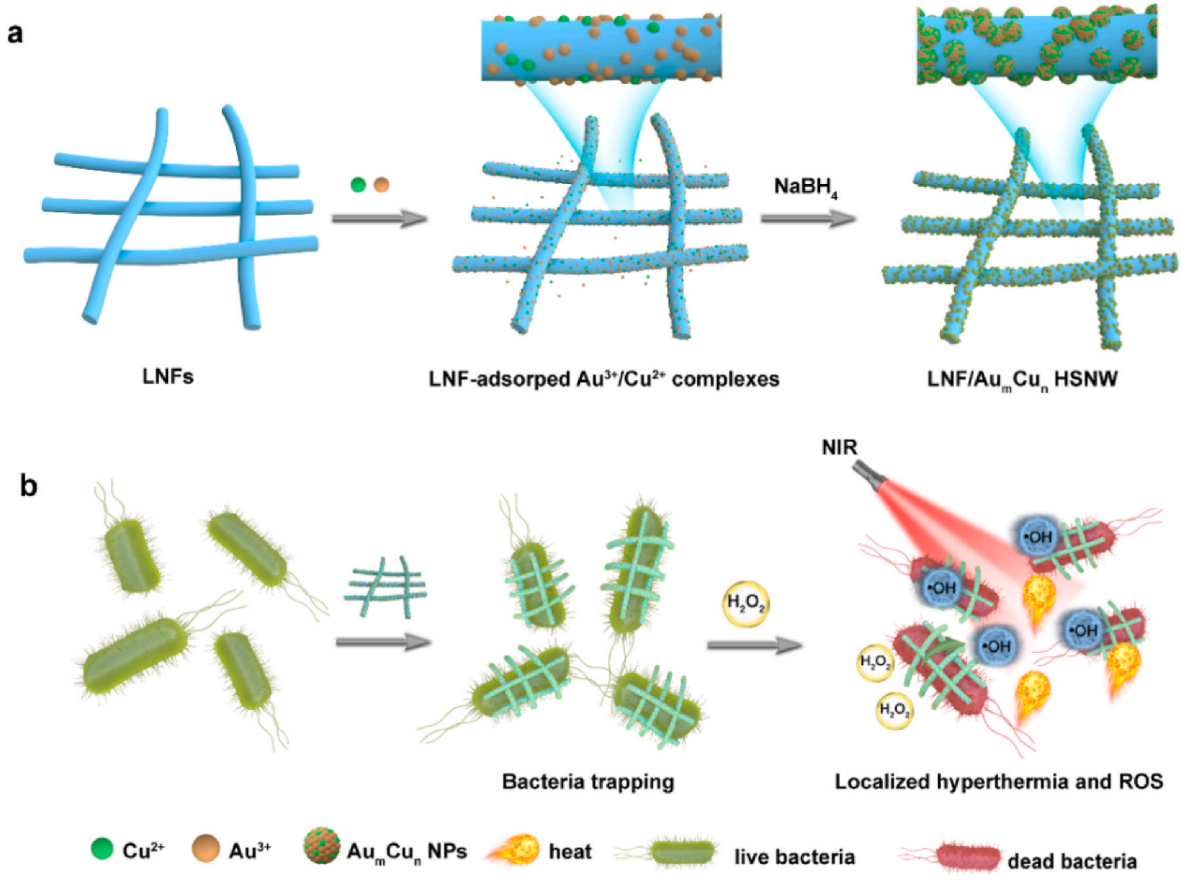

Scheme 1. LNF/Au_mCu_n HSNW synthesis procedure and biomimicking catalytic antibacterial therapy. (a) Schematic illustration of LNF/Au_mCu_n HSNW synthesis. (b) Bactericidal efficiency of LNF/Au_mCu_n HSNW synergistically enhanced by its bacteria trapping and NIR stimulus.

3. Results and discussion

3.1. Preparation and characterizations of LNF/Au_mCu_n HSNW

Scheme 1 depicts the synthesis procedure of bimetallic LNF/Au_mCu_n HSNW, and it is also similar for monometallic LNF/Au (as the control). First, LNFs were prepared by the incubation of lysozyme monomer in eutectic solvent composed of the mixture of hydrochloric acid-glycine solution and acetic acid-choline chloride solution (v/v = 19/1). After redispersed in water to form LNFs suspension, metal ions were added subsequently and incubated for 0.5 h to fully form metal ion and LNFs complexes through multiple interactions between metal ions and residues of lysozyme consisted of 139 amino acids (18 types of amino acids). Therefore, LNF confined monometallic Au or bimetallic Au_mCu_n hybrid supramolecular fibrous networks were obtained after the reduction of metal ions with different ratios of Au^{3+}/Cu^{2+} by $NaBH_4$ for 10 min.

The transmission electron microscopy (TEM) image (Fig. 1a) shows the typical fibril-like structure of LNF/Au_3Cu_1 HSNW, along with a number of ultrasmall NPs densely and orderly allied on the surfaces of LNFs, which can be ascribed to the excellent space confinement of 1D fibrous structure with an average diameter of 11.2 nm (Fig. S1), and the inherently strong metal ion chelation, particularly the formation of Au–S bonds [33]. Consequently, ultrafine monometallic Au or bimetallic Au_mCu_n NPs with narrow size distribution can regularly grow and scatter on the LNF surfaces (Fig. 1c and Fig. S2). Compared to that of Au NPs, the Au_mCu_n NPs possess smaller particle sizes (2.2–3.0 nm vs 4.5 nm), which can be ascribed to the different reduction rate of Au^{3+} and Cu^{2+} ions during the co-reduction process [34], where the Cu^{2+} ions with stronger oxidation capacity can be reduced faster, effectively inhibiting the fast growth of Au NPs, thus resulting in smaller Au_mCu_n NPs. From the high-resolution TEM (HRTEM) image (Fig. 1b), it is observed that the ultrafine NPs on the LNF/Au_3Cu_1 surfaces are dominantly single crystalline structure with the lattice spacing of ca. 0.233 nm, close to that of the alloyed Au_3Cu_1 (111) plane, and no metallic Cu^0 lattice spacing is observed. In addition, Fig. 1d–k shows the high-angle annular dark-field scanning transmission electron microscopy (HADDF-STEM) images of LNF/Au_3Cu_1 and the corresponding element mappings of Au, Cu, C, N, S, and O, particularly the Au signal (Fig. 1e) and Cu signal (Fig. 1f) share a similar dispersion region and can be well merged together (Fig. 1g), suggesting their alloying interaction.

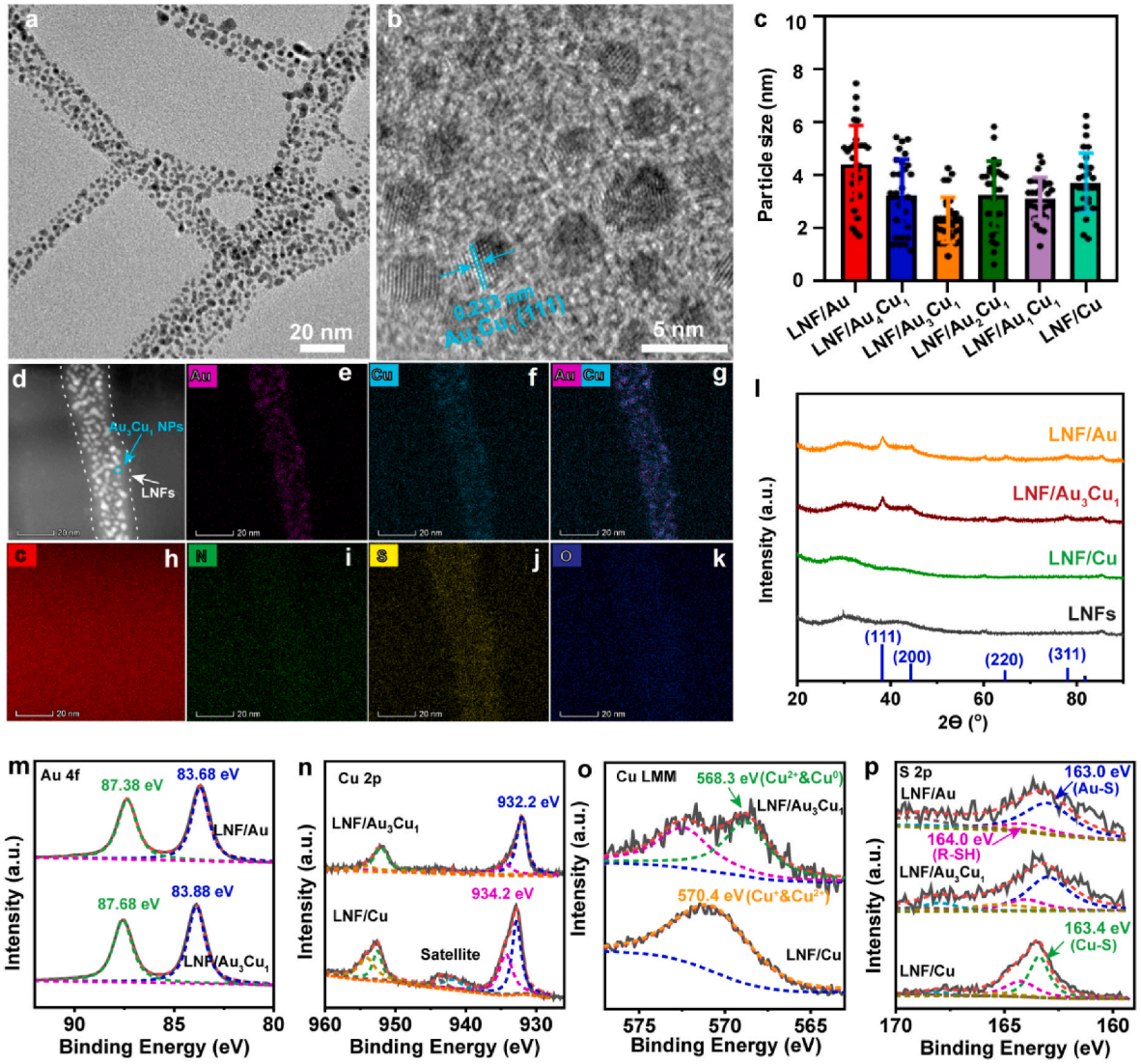

Fig. 1. Morphology and structure characterizations of LNF/Au_mCu_n HSNW. (a) TEM image of LNF/Au_3Cu_1 HSNW. (b) HRTEM image of LNF/Au_3Cu_1 HSNW. (c) Average particle sizes of metal NPs on LNF/Au_mCu_n HSNW with different Au/Cu ratios. (d) HADDF-STEM image of LNF/Au_3Cu_1 HSNW. (e–k) STEM-Mapping images of Au, Cu, C, N, S, O of LNF/Au_3Cu_1 HSNW. h is the merged Au and Cu element. (l) XRD patterns of LNF/Au_mCu_n HSNW. (m) Au 4f XPS spectra of LNF/Au and LNF/Au_3Cu_1 HSNW. (n) Cu 2p XPS spectra of LNF/Au and LNF/Au_3Cu_1 HSNW. (o) Cu LMM AES spectra of LNF/Au and LNF/Au_3Cu_1 HSNW. (p) Au 4f XPS spectra of LNF/Au and LNF/Au_3Cu_1 HSNW.

Meanwhile, the presence of C, N, S, and O signals, especially the strong S signal with a 1D fibril-like and broader dispersion than that of Au or Cu signal (Fig. 1j), reveal the LNFs well maintain their supramolecular fibrillar structure after binding metal NPs.

The X-ray diffraction (XRD) pattern of LNF/Au_3Cu_1 shows four characteristic peaks at 2θ = 38.15, 44.35, 64.6, 77.8°, which can be indexed as the (111), (200), (220), (311) planes of fcc Au_3Cu_1 alloys (JCPDS NO. 34–1302), and three other peaks at 2θ = 29.6, 60.3, 85.5° can be assigned to the characteristic peaks of XRD pattern of the LNFs. No characteristic peaks are ascribed to crystalline Cu^0 or copper oxide, implying that the copper species could be well alloyed with the gold species to form the bimetallic Au_3Cu_1 nanocrystals. It is noteworthy that the XRD pattern of LNF/Au is similar to that of LNF/Au_3Cu_1, revealing their similar crystalline structure, which is consistent with the HRTEM

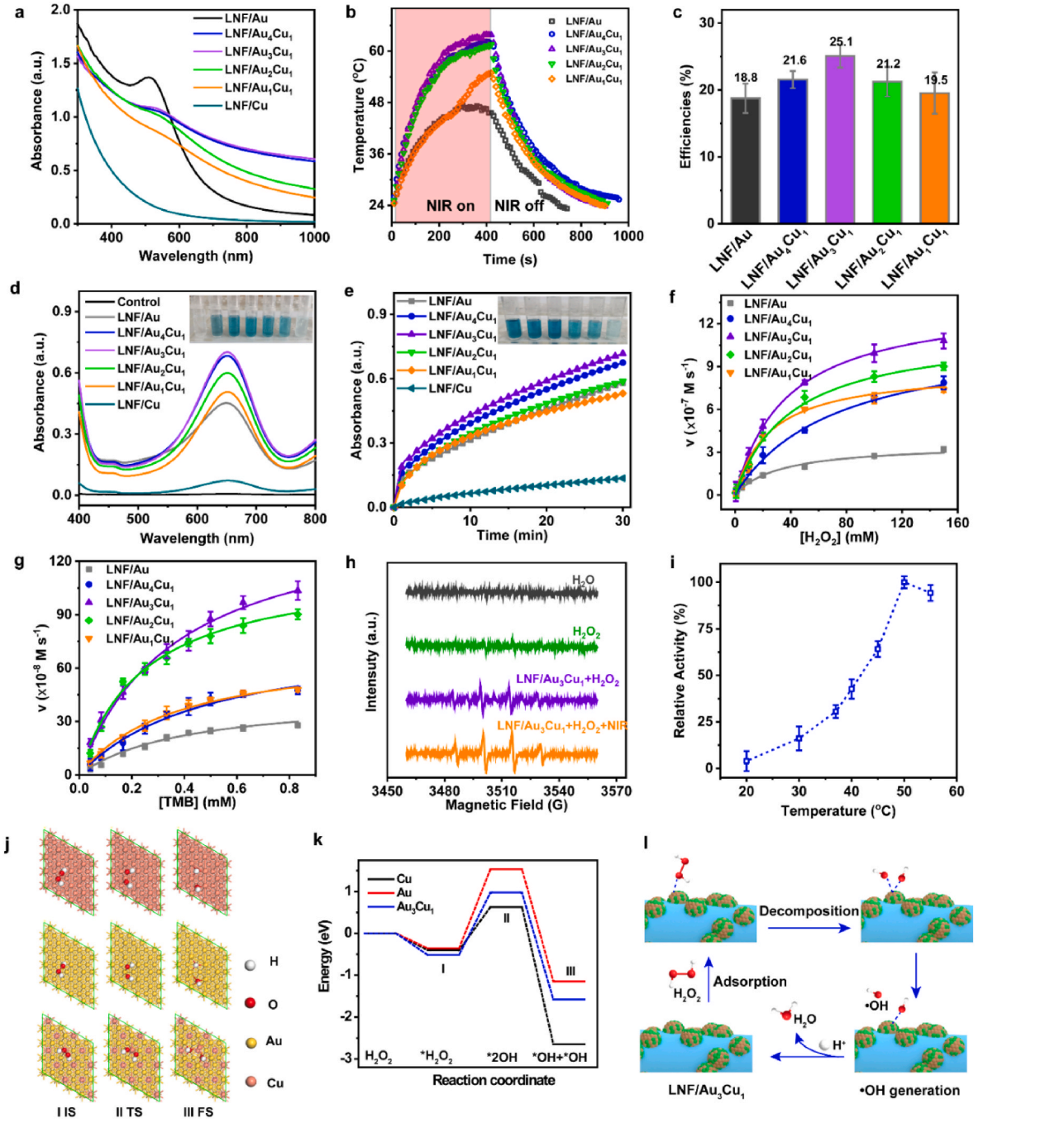

Fig. 2. Enhanced photothermal activity and POD-like activity of LNF/Au_mCu_n HSNW. (a) UV–Vis–NIR absorption spectra of different LNF/Au_mCu_n HSNW. (b) Heating and cooling curves of different LNF/Au_mCu_n HSNW with or without NIR irradiation (808 nm, 2 W cm^{-2}). (c) Photothermal conversion efficiencies of different LNF/Au_mCu_n HSNW. (d) UV–vis absorption spectra of TMB oxidation catalyzed by different LNF/Au_mCu_n HSNW with H_2O_2 as substrate. (e) Time-dependent absorbance of ox-TMB in different groups. The insets are the corresponding visual color changes. (f) Steady-state kinetic assay of LNF/Au_mCu_n for H_2O_2. (g) Steady-state kinetic assay of LNF/Au_mCu_n for TMB. (h) ESR spectra demonstrating ·OH generation under different conditions. (i) Relative activities of LNF/Au_3Cu_1 with TA as indicator under different temperatures. (j) Structure models of monometallic Cu(111), Au (111) and bimetallic Au_3Cu_1 (111) planes interact with different intermediates. (k) Free energy diagrams of POD-like catalysis over Cu(111), Au (111) and Au_3Cu_1(111) planes. (l) Proposed mechanism of LNF/Au_3Cu_1 HSNW catalyzing the decomposition of H_2O_2 into •OH. (For interpretation of the references to color in this figure legend, the reader is referred to the Web version of this article.)

results (Fig. 1b and Fig. S3). To distinguish their difference, X-ray photoelectron spectroscopy (XPS) was further performed. For the XPS survey spectra of LNF/Au_mCu_n, characteristic peaks of Au and Cu species clearly present with the content-dependent intensities (Fig. S4), whereas for LNF/Au or LNF/Cu, only Au or Cu characteristic peaks are observed. More information was obtained from the high resolution Au4f, Cu2p3/2, Cu LMM, and S2p spectra with LNF/Au, LNF/Au_3Cu_1, and LNF/Cu as the representative samples. As shown in Fig. 1m, the Au4f spectrum of LNF/Au_3Cu_1 shows two peaks at 83.88 and 87.68 eV, derived from $Au4f_{7/2}$ and $Au4f_{5/2}$ respectively, significantly shifting to higher binding energy compared to that of LNF/Au, which can be attributed to the introduction of Cu species leading to the electrons transfer from Au to Cu species, being consistent with previously results of Au_3Cu_1 alloy [35]. Moreover, for the $Cu2p_{3/2}$ spectra of LNF/Au_3Cu_1 and LNF/Cu (Fig. 1n), two peaks at 932.2 eV and 934.2 eV can be deconvoluted, assigned to metallic Cu^0 and oxidative Cu^{2+}, respectively. As for the $Cu2p_{3/2}$ spectrum of LNF/Au_3Cu_1, the peak located at 932.2 eV is absolutely higher and no satellite is observed, suggesting the copper species in LNF/Au_3Cu_1 are mainly metallic Cu^0 [35], and the observed small peak of Cu^{2+} species may be derived from the formation of Cu–S bond due to the strong chelation of LNFs. In contrast, the peak of the $Cu2p_{3/2}$ spectrum for LNF/Cu shifts to higher binding energy, especially the presence of satellite, indicating more copper species with high oxidative states (Cu^{2+} or Cu^{+}), which could be attributed to the easy oxidation of monometallic Cu^0 NPs exposed in water. The Auger electron spectra (AES) of Cu LMM for LNF/Au_3Cu_1 (Fig. 1o) displays a characteristic peak around 568.3 eV, further confirming the presence of Cu^0 and Cu^{2+} species [36], whereas for LNF/Cu only one broad peak around 570.4 eV is observed, demonstrating the copper species are mainly Cu^{+} species [36]. Fig. 1p shows the S2p spectra of LNF/Au and LNF/Au_3Cu_1 can be deconvoluted into two peaks at 164.0 and 163.0 eV, corresponding to R–SH and Au–S bonds, respectively [37]. In addition, characteristic peak of Cu–S bond around 163.4 eV can be deconvoluted for the $S2p_{3/2}$ spectrum of LNF/Cu [37]. It is suggested that there is strong interaction between the metal NPs and the LNFs through the Au–S or Cu–S bonds, which is important for stabilizing the bimetallic Au and Cu NPs on the LNF surfaces. The C1s, N1s, and O1s spectra mainly originating from the C, N, O elements of LNFs for LNF/Au, LNF/Au_3Cu_1, and LNF/Cu are similar, demonstrating the well hybrids of metal NPs and LNF. Furthermore, the detected Au and Cu atom ratios in the bimetallic LNF/Au_mCu_n by XPS are close to those of the quantitative Au/Cu ratio measured by inductively coupled plasma-optical emission spectrometer (ICP-OES) (Table S1).

3.2. Photothermal conversion performance of LNF/Au_mCu_n HSNW

Next, the plasmonic features of LNF/Au_mCu_n HSNW are further explored, and Fig. 2a shows the ultraviolet–visible (UV–Vis) absorption spectra of LNF/Au_mCu_n HSNW with different Au/Cu ratios. As for monometallic LNF/Au, the sharp surface plasmon peak around 515 nm demonstrates the formation of metallic Au NPs. Meanwhile, it displays broad absorption in the range from 700 to 1000 nm, which can be attributed to the alliance of Au NPs confined by the 1D LNF [30]. The bimetallic LNF/Au_mCu_n HSNW exhibit the surface plasmon peak at 535 nm, between that of Au (520 nm) and Cu (570 nm), confirming the alloying structure and presence of Au and Cu NPs, which is consistent with previous results [38]. Moreover, the Au and Cu alloying structure, especially for LNF/Au_4Cu_1 and LNF/Au_3Cu_1, remarkably promotes the near infrared (NIR) absorption (700–1000 nm). It is noted that no characteristic surface plasmon peak (570 nm) is observed for the LNF/Cu spectrum, suggesting no metallic Cu presented in the LNF/Cu HSNW, consistent with the results of XRD and XPS analysis. This may be attributed to the easy oxidization of ultrasmall Cu^0 NPs in water because of their inherently high activity. Taking advantage of their excellent NIR absorption, the temperatures of LNF/Au_mCu_n HSNW suspensions can be obviously increased from room temperature to the maximum temperatures of 48.5, 61.7, 64.2, 61.4, 54.0 °C for LNF/Au, LNF/Au_4Cu_1, LNF/Au_3Cu_1, LNF/Au_2Cu_1, LNF/Au_1Cu_1 HSNW, respectively (Fig. 2b) under the 808 nm NIR light irradiation for 400 s. The corresponding photothermal conversion efficiencies were determined to be 18.8%, 21.6%, 25.1%, 21.2%, and 19.5% (Fig. 2c), suggesting the Au/Cu ratio significantly affects the photothermal activity of LNF/Au_mCu_n HSNW. This can be attributed to the intrinsic strong interaction between Au and Cu in the Au_mCu_n alloying NPs, varying their local surface plasmonic resonance (LSPR) absorbance band [39]. With an optimal Au/Cu ratio of 3/1, the LNF/Au_3Cu_1 HSNW has the strongest LSPR absorbance around 808 nm, thus offering the highest photothermal conversion efficiency when it is irradiated by an 808 nm laser. It is noteworthy that most photothermal nanomaterials, especially for noble-metal nanostructures (e.g., Au nanorods), with large size (>20 nm) and high stability, are hard to be degraded or removed by human body. In contrast, ultrasmall NPs (<5 nm) can be easily removed by the renal cycling, thus showing high biosafety. Considering the high photothermal conversion efficiency and the unique structure composed of ultrasmall NPs, the LNF/Au_mCu_n, especially for LNF/Au_3Cu_1 HSNW, would be used as novel and biocompatible photothermal nanoagents.

3.3. POD-like catalytic performance of LNF/Au_mCu_n HSNW

Importantly, the catalytic reaction of LNF/Au_mCu_n HSNW as the novel POD-like nanozyme has been examined. The typically chromogenic reaction of 3,3′,5,5′-tetramethylbenzidine (TMB) oxidation catalyzed by resultant LNF/Au_mCu_n HSNW with the introduction of H_2O_2 was used to investigate their intrinsic POD-like activity (inset of Fig. 2d). Note the absorbance values of the oxidized TMB (ox-TMB) catalyzed by the bimetallic LNF/Au_mCu_n HSNW are higher than those of monometallic LNF/Au or LNF/Cu (Fig. 2d), demonstrating their enhanced POD-like activity. Among those LNF/Au_mCu_n HSNW, the LNF/Au_3Cu_1 HSNW exhibits the highest absorbance value, suggesting the best POD-like activity. Fig. 2e further demonstrated the LNF/Au_3Cu_1 HSNW could still maintain the highest catalytic activity with prolonging the reaction times. The Michaelis−Menten kinetics was employed to study the catalytic property of LNF/Au_mCu_n HSNW (Fig. 2f and g). The calculated kinetics parameters are listed in Table S2. Among the LNF/Au_mCu_n HSNW, when using H_2O_2 as a substrate, the LNF/Au_3Cu_1 HSNW exhibits the smallest K_m value (15.94 mM), and the largest maximum rate (V_{max}) (8.3×10^{-7} M s^{-1}) indicating the best affinity toward H_2O_2 and catalytic performance. While using TMB as a substrate, the smallest K_m value of 0.24 mM for LNF/Au_3Cu_1 HSNW demonstrates it also has the best TMB binding affinity. The V_{max} values of TMB for LNF/Au_mCu_n HSNW are in an order of LNF/Au_2Cu_1 (19.2) > LNF/Au_3Cu_1 (12.4) > LNF/Au_4Cu_1 (8.6) > LNF/Au_1Cu_1 (7.6) > LNF/Au (6.7), suggesting that the bimetallic LNF/Au_mCu_n HSNW show higher TMB oxidation rate than monometallic LNF/Au HSNW, probably due to the introduction of more active copper species than gold species for the Fenton reaction. Therefore, increasing the copper content in LNF/Au_mCu_n HSNW is beneficial for promoting the TMB oxidation, but excessive copper content (Au/Cu = 1/1) can reduce their activity. In this case, it is very important to control the Au/Cu ratio of LNF/Au_mCu_n HSNW for optimizing the best nanozyme. Compared to the kinetic parameters of commercial Fe_3O_4 (K_m of 62.5 mM and V_{max} of 0.58×10^{-7} M s^{-1} towards H_2O_2), all the LNF/Au_mCu_m HSNWs exhibit smaller K_m and higher V_{max} values, resulting in much better affinity and higher catalytic performances. Although the lower K_m values of natural HRP demonstrates it has better affinity towards H_2O_2 and TMB than those of LNF/Au_mCu_n HSNW, its much lower V_{max} and K_{cat} values indicates its relatively much lower catalytic performances in comparison (Table S2). Electron paramagnetic resonance (EPR) was further performed to probe the catalytic conversion of H_2O_2 into •OH by LNF/Au_3Cu_1 HSNW. Fig. 2h clearly shows the •OH signal when LNF/Au_3Cu_1 HSNW was introduced into the H_2O_2 solution. More importantly, upon NIR irradiation, the •OH signal can be significantly enhanced, about 1.5 times higher than that without NIR

irradiation (Fig. 2h). This enhancement is further demonstrated by the catalytic oxidation of nonfluorescent terephthalic acid (TA), an indicator for detecting •OH, into fluorescent 2-hydroxy terephthalic acid (HTA). Fig. S5 clearly shows after NIR irradiation, the fluorescence intensity of HTA is obviously enhanced as compared to that without NIR treatment, meaning more generated •OH available, which can be attributed to the photothermal effect of LNF/Au_3Cu_1 HSNW triggering the temperature elevation. Thus, we subsequently determined the effect of temperature on the catalytic activity of LNF/Au_3Cu_1 HSNW using the TA oxidation reaction. It is clearly shown in Fig. 2i, the relative catalytic activity is increased from 20 to 48 °C, but then decreased with further increasing the temperature to 55 °C. Moreover, it is found that in acidic medium the LNF/Au_3Cu_1 HSNW exhibited higher catalytic activity than that in neutral medium, giving the best catalytic performance at pH around 3 (Fig. S6), which provided the basis for catalytic killing bacteria in the infected wound with the acidic micro-condition. In general, the results demonstrate the bimetallic LNF/Au_3Cu_1 HSNW displays higher H_2O_2 affinity and catalytic activity than the monometallic LNF/Au HSNW, which significantly depends on the temperature and pH and can be remarkably enhanced by external NIR stimulus.

3.4. Catalytic mechanism of LNF/Au_3Cu_1 HSNW

To further explore the enhanced enzyme-like activity of bimetallic LNF/Au_3Cu_1 HSNW as compared to monometallic LNF/Au HSNW, density functional theory (DFT) calculations were conducted to simulate the catalytic mechanism. The computational details are provided in the supporting information. For metal nanozymes, the metal NPs are the active component for activating the enzyme-like catalytic reaction. Thus, as for the monometallic LNF/Au and bimetallic LNF/Au_3Cu_1, it is certainly believed that metallic Au and Au_3Cu_1 NPs supported on LNF are the active components. Based on the results of HRTEM images (Fig. 1 and Fig. S3) and XRD (Fig. 1l) analysis, Au (111) and Au_3Cu_1 (111) planes are dominantly exposed on the surfaces of Au and Au_3Cu_1 NPs. Therefore, it is reasonable to build Au (111), Cu(111) and Au_3Cu_1 (111) planes as the model catalysts for catalyzing the H_2O_2 decomposition (Fig. 2j). The reaction of H_2O_2 decomposition into •OH catalyzed by Cu, Au, or Au_3Cu_1 planes was supposed to follow a three-steps pathway [40] as depicted in Fig. 2j. The H_2O_2 molecules are first adsorbed by Cu(111), Au (111), or Au_3Cu_1(111) planes, forming $*H_2O_2$, where the asterisk (*) can be considered as the catalyst. This initial step (I, IS) is very important for the activation of H_2O_2 molecules. Then, the activated $*H_2O_2$ is homogenously dissociated into two hydroxyl groups at one single active site (*2OH), which can be the key transition step (II, TS) for the formation of hydroxyl radicals. Finally, one of the two hydroxyl groups desorbs from the adsorbed site to form the hydroxyl radical (•OH). The generated •OH can be easily re-adsorbed by another active site of the catalyst to form another hydroxyl group intermediate (*OH) if it doesn't react with other substrates. Thus, it can be considered as the final step for the reaction of H_2O_2 decomposition (III, FS). Fig. 2k shows the corresponding free energy diagrams of the H_2O_2 decomposition catalyzed by Cu (111), Au (111), or Au_3Cu_1 (111) planes. Comparing with monometallic Cu and Au, the bimetallic Au_3Cu_1 exhibits the lowest adsorption energy towards H_2O_2 (−0.515 eV), indicating the highest capacity of H_2O_2 adsorption. Moreover, the homogeneous dissociation of H_2O_2 into hydroxyl groups can be the rate determining step (RDS) with the energy barriers of 0.632, 1.534, and 0.976 eV for Cu, Au and Au_3Cu_1 models, respectively. It is observed that the bimetallic Au_3Cu_1 as active sites exhibit higher POD-like activity than Au alone, which can be attributed to the introduction of the more active metallic Cu into the bimetallic Au_3Cu_1 due to the lowest energy barrier of Cu. Thus, the enhanced POD-like activity for LNF/Au_3Cu_1 can be attributed to the higher capacity of adsorbing H_2O_2 molecules (lower absorption energy) and faster •OH generation (lower energy barrier) for Au_3Cu_1 active sites as compared to those for LNF/Au. It is worthy to note that the LNF/Cu might possess the highest POD-like activity due to the metallic Cu owing the lowest energy barrier in theory, but it displays the lowest activity in the practical catalytic H_2O_2 decomposition, which can be attributed to no metallic Cu^0 observed in the LNF/Cu due to their instability as declared by XPS and XRD analysis.

Therefore, based on the above experimental and theoretical calculation results, a reasonable reaction route of LNF/Au_3Cu_1 HSNW catalyzing H_2O_2 decomposition into •OH under acidic condition was proposed (Fig. 2l). The Au_3Cu_1 active sites exposed on LNF surfaces first interact with the H_2O_2 molecules and activate them. Subsequently, the H_2O_2 molecules decompose homogeneously to form two hydroxyl groups, one of which desorbs to form the hydroxyl radicals that could trigger the oxidation of a series of substrates (e.g., TMB, TA, proteins, DNA, peptides, etc.). The other finally reacts with H^+ derived from the acidic mediate to form the H_2O molecules. During the reaction, besides the synergic effect between Au and Cu in Au_3Cu_1 alloying structure, the strong binding interaction between the LNF and Au_3Cu_1 NPs also plays an important role in promoting the catalytic reaction due to their electron transfers [32].

3.5. Antibacterial performance of LNF/Au_3Cu_1 HSNW

The POD-like catalytic performance of LNF/Au_3Cu_1 HSNW has been well evaluated, and it could be further applied in catalytic antibacterial therapy with overwhelming superiority of reducing the amount of H_2O_2, which is a common reagent for disinfection, but the inhibitory concentrations could be 3–18 mM, hampering wound healing and even damaging normal tissues [41]. In contrast, •OH derived from the catalytic decomposition of H_2O_2 by LNF/Au_3Cu_1 HSNW can be much more effective for killing bacteria with the H_2O_2 concentration only ranging from 0.1 to 0.5 mM, which is less than thirtieth of inhibitory concentration of H_2O_2. Meanwhile, combined with the photothermal activity of LNF/Au_3Cu_1 HSNW and the fibrillar network structure, they potentially contribute to the excellent antibacterial properties. As shown in Fig. S6, it confirms that H_2O_2 alone at concentrations of 100–500 μM hardly kills the bacteria, including *E. coli* and *S. aureus* as the Gram-negative and Gram-positive bacteria, respectively. In contrast, the introduction of LNF/Au_3Cu_1 HSNW at a metal concentration of ca. 80 μg mL^{-1}, with non-cytotoxicity (Fig. S7), could kill the bacteria with the viabilities decreased obviously (<30%), especially at the concentration of H_2O_2 >200 μM, which can be attributed to the catalytic production of •OH. It is noteworthy that *S. aureus* possess thicker cell wall than *E. coli*, making them more tolerable to •OH, so that it requires higher H_2O_2 concentration to achieve similar bactericidal efficiency as compared to that for *E. coli* (Fig. S6). For instance, as shown in Fig. 3a–b, when the bacteria are treated with LNF/Au_3Cu_1 HSNW at 100 μM H_2O_2 for 8 min (**group III**), the viabilities of *E. coli* and *S. aureus*, calculated on the basis of the corresponding plate count method (Fig. 3c and d), are 48.3% and 54.8%, respectively. Nevertheless, under NIR irradiation (808 nm, 1.5 W cm^{-2}) (**group V**), the bacterial viabilities are remarkably decreased to be about 0%, demonstrating neither *E. coli* nor *S. aureus* are survived, which can be attributed to the synergy between the enhanced •OH production with external NIR stimulus, and the localized photothermal ablation generated by LNF/Au_3Cu_1 HSNW. This can be proved by group IV that upon NIR irradiation the LNF/Au_3Cu_1 HSNW can heat the bacteria suspension (ca. 48 °C) and kill part of the bacteria, giving corresponding viabilities of *E. coli* and *S. aureus* of 56.3% and 43.8%, respectively. No obvious bacterial inhibition is observed for the treatments of group II, VI, and VII, indicating single LNF/Au_3Cu_1 HSNW (80 μg mL^{-1}), NIR (808 nm, 1.5 W cm^{-2}), or H_2O_2 (100 μM) treatments for 8 min hardly affect the bacterial viabilities.

To further demonstrate the antibacterial performances of LNF/Au_3Cu_1 HSNW, the variations of bacterial morphology were observed by scanning electron microscope (SEM). As shown in Fig. 3e and f, for control (**group I**), both *E. coli* and *S. aureus* exhibit intact cell wall with smooth surfaces, while incubated with LNF/Au_3Cu_1 HSNW (**group II**), it is observed that the whole bacterial surfaces are almost covered by

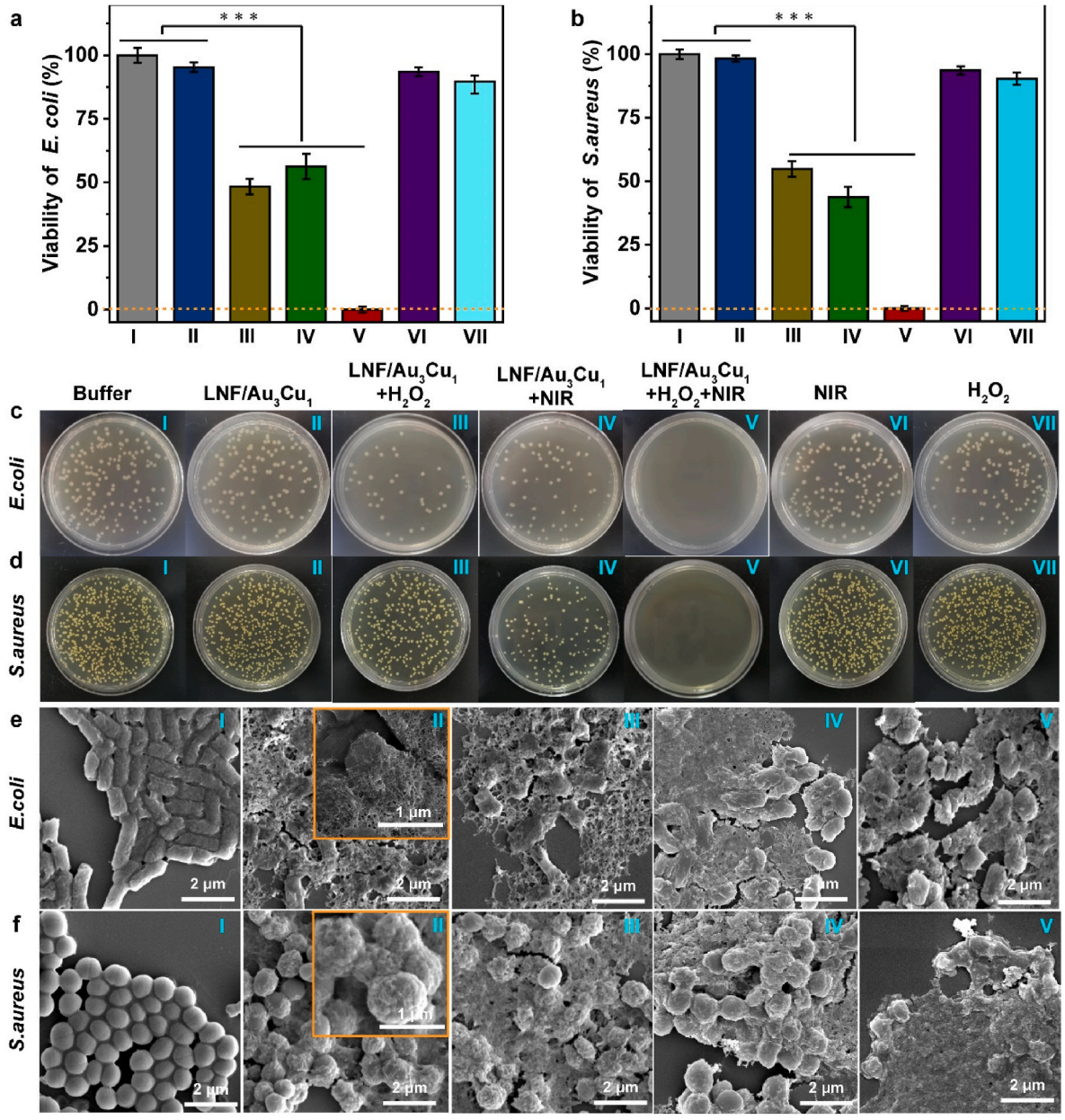

Fig. 3. Catalytic antibacterial performances of LNF/Au_3Cu_1 HSNW. (a) Viability of *E. coli* treated under different conditions. (b) Viability of *S. aureus* treated under different conditions. (c) Photographs of *E. coli* colonies growth by spread plate method. (d) Photographs of *S. aureus* colonies growth by spread plate method. (e) SEM images of *E. coli* treated under different conditions. (f) SEM images of *S. aureus* treated under different conditions. Conditions: (I) NaAc-HAc (pH = 5.5); (II) Bacteria incubated with LNF/Au_3Cu_1 HSNW; (III) Bacteria treated with LNF/Au_3Cu_1 HSNW and H_2O_2; (IV) Bacteria treated with LNF/Au_3Cu_1 HSNW under NIR irradiation. (V) Bacteria treated with LNF/Au_3Cu_1 HSNW and H_2O_2 under NIR irradiation; (VI) Bacteria treated with NIR irradiation alone; (VII) Bacteria treated with H_2O_2 alone. Data were expressed as mean ± SDs (n = 3). $^*p < 0.05$, $^{***}p < 0.001$.

fibril-like materials, which can be ascribed to the strong adherence of LNF/Au_3Cu_1 HSNW towards the bacterial surfaces, but they hardly impact the bacterial morphologies since the intact and smooth surfaces of the bacteria are still maintained. However, after the addition of H_2O_2 **(group III)**, the bacterial surfaces become wrinkly and rough but the bacteria can still maintain their original cell morphology, which can be caused by the attack of •OH. As for LNF/Au_3Cu_1 HSNW upon NIR irradiation (**group IV**), the single heat treatment triggered by LNF/Au_3Cu_1 HSNW also causes the wrinkle and rough of the bacteria surfaces, and even some holes generated on the surfaces of *E. coli*, suggesting the different damages to bacteria between heat and •OH attacks, but the cell membrane integrity can be maintained as well. For bacteria treated by the combination of catalytic and photothermal actions **(group V)**, it is clearly observed that the cell membrane integrities of both *E. coli* and *S. aureus* cannot be maintained any more, becoming rather wrinkly, and some are even broken, indicating a much stronger antimicrobial performance compared to that of single catalytic or photothermal actions, thus resulting in completely bacterial death.

The bacterial interaction and enhanced damages to bacterial membranes of LNF/Au_3Cu_1 HSNW are further investigated by the TEM and SYTO 9/PI staining fluorescence analyses (Figs. S8, S9, S10). Fig. S9b clearly shows the *S. aureus* surfaces are covered by a number of nanofibrils when they incubated with LNF/Au_3Cu_1 HSNW, which is consistent with the SEM analysis. In contrast, the *S. aureus* surfaces are only decorated with a few particulates when they incubated with pure Au_3Cu_1 nanoparticles prepared without LNF as the template (Fig. S8c). Compared to the small and well dispersed green fluorescent spots in Fig. S10a, the presence of large green fluorescent spots in Fig. S9b

further demonstrates the strong aggregation of the bacteria due to the strong bacterial adhesion of LNF/Au_3Cu_1 HSNW. Fig. S10 show the TEM images of *S. aureus* treated by single mode of catalysis (Fig. S10b) and dual modes of catalysis and PTT (Fig. S10c), respectively. Fig. S10a clearly shows normal *S. aureus* have clean, intact and spherical cell membranes. After single POD-like catalysis treatment, the bacterial cell membranes become ambiguous but their integrity still maintains (Fig. S10b). However, with the treatment of POD-like catalysis and PTT, the cell membranes of *S. aureus* become wrinkle and even holes generate (Fig. S10c), demonstrating more serious damages occur on bacterial surfaces compared to that with catalysis treatment alone. The red fluorescent spots present in Fig. S9c further confirms the membrane rupture of the *S. aureus* because the PI dye can interact with the DNA inside the bacteria.

3.6. Antibacterial mechanism of LNF/Au_3Cu_1 HSNW

On basis of the above results, a possible antibacterial mechanism of LNF/Au_3Cu_1 HSNW killing bacteria have been proposed, as depicted in Scheme 1b. Owing to the intrinsic soft, fine and long fibrous nanostructure of LNF, the LNF/Au_3Cu_1 HSNW can strongly bind with the bacteria surfaces when they meet the bacteria. After the addition of H_2O_2, the H_2O_2 molecules can be adsorbed and decomposed into the highly active •OH due to the high POD-like activity of the ultrafine Au_3Cu_1 NPs on LNF/Au_3Cu_1 HSNW. Subsequently, the generated •OH are able to locally and directly attack the bacterial membranes, causing a series of oxidative damages. Particularly, with external NIR stimulation, the LNF/Au_3Cu_1 HSNW is capable of absorbing the light and generate plentiful hot carriers, which can combine with the ROS to synergistically enhance the damages of the bacterial membranes, meanwhile the accompanying thermal effect certainly accelerates the H_2O_2 conversation into •OH, further increasing the damages to the bacteria (Fig. 3e, f and Fig. S10c), and finally leading to the complete death of the bacteria (Fig. S10c).

3.7. Infected wound healing performance of LNF/Au_3Cu_1 HSNW

It is noted that *methicillin-resistant S. aureus* (*MRSA*) show strong resistance to oxacillin but they hardly survive when treated with LNF/Au_3Cu_1 HSNW in the presence of H_2O_2 and NIR irradiation (Fig. S11). In addition, Fig. S12 indicates that the LNF/Au_3Cu_1 HSNW hardly shows any cytotoxicity to normal cells. Therefore, to further demonstrate LNF/Au_3Cu_1 HSNW can be an efficient smart nanozyme against AMR associated infection, a MRSA infected mouse wound model was used to evaluate the disinfection performance *in vivo* and wound healing treated by LNF/Au_3Cu_1 HSNW, which follows a procedure as depicted in Fig. 4a. The mice with a back wound diameter of ca. 8 mm were randomly divided into 7 group: PBS, LNF/Au_3Cu_1, LNF/Au_3Cu_1+H_2O_2, LNF/Au_3Cu_1+NIR, LNF/Au_3Cu_1+H_2O_2+NIR, NIR, H_2O_2. The wound healing process were monitored for 14 days (Fig. 4b). As shown in Fig. 4b–d, better crusting is observed on 3 days for the LNF/Au_3Cu_1+H_2O_2+NIR group than for the other groups. Particularly, on day 7, scars are formed for all groups but the wound size of LNF/Au_3Cu_1+H_2O_2+NIR group presents the smallest, only 11.1% of day 0. By contrast, the wound sizes for the LNF/Au_3Cu_1+H_2O_2 and LNF/Au_3Cu_1+NIR treatments are 20% and 28%, respectively, while for the PBS, LNF/Au_3Cu_1, NIR, and H_2O_2 groups, the wound sizes are higher than 32% (Fig. 4d and Fig. S13). The wound almost completely vanishes on day 14 for the LNF/Au_3Cu_1+H_2O_2+NIR group, while obvious wound border and dermal incompleteness can still be seen in other groups (Fig. 4b). Fig. 4c–e shows the H_2O_2, NIR, and LNF/Au_3Cu_1 groups hardly kill the *MRSA* on the wounds (>96% viability), while the MRSA viabilities for LNF/Au_3Cu_1+H_2O_2, LNF/Au_3Cu_1+NIR, LNF/Au_3Cu_1+H_2O_2+NIR groups are significantly reduced, giving 16.2%, 26%, and 1.6%, respectively, which can be attributed to their excellent antibacterial properties. The complete death of MRSA for LNF/Au_3Cu_1+H_2O_2+NIR treatment verifies the enhanced *in vivo* antibacterial efficiency for the combination of nanozyme catalysis and PTT. In order to further verify the wound healing, we used hematoxylin and eosin staining (H&E staining) to analyze the tissue sections of the wound. As shown in Fig. 4f, the wounds treated with LNF/Au_3Cu_1+H_2O_2+NIR exhibits complete epidermis layer, revealing the good healing, whereas fragmented epidermis layer and even obvious tissue breakage are observed for other group, indicating their poor wound healing efficiency. Furthermore, immunohistochemistry staining was used to detect the expression of proliferating nuclear antigen protein PCNA. It is found that the expression level of PCNA in the untreated group is low. For the LNF/Au_3Cu_1+H_2O_2+NIR treatment, the number of PCNA-positive cells is enhanced. Compared to other groups, LNF/Au_3Cu_1+H_2O_2+NIR treatment could proliferative activity of cells within the skin tissue, especially for the basal cells that can promote the proliferation and metabolism of keratinocytes, and the positive expression of PCNA is enhanced (Fig. 4g). Furthermore, a histological analysis of the main organs was done after treatment (Fig. S14). The H&E staining images of the heart, liver, spleen, lung, and kidney for the LNF/Au_3Cu_1+H_2O_2+NIR treatment groups show no obvious histological changes compared to those of healthy mice, suggesting the safe application of LNF/Au_3Cu_1 HSNW for the treatment of infectious wounds. This can be attributed to the intrinsic good stability (Fig. S15a) and biodegradability of LNF/Au_3Cu_1 HSNW since it can be easily degraded into ultrasmall bimetallic NPs and lysozyme monomers by protease (Fig. S15b). Therefore, it can be concluded that with the adjuvant of H_2O_2 and NIR irradiation, the LNF/Au_3Cu_1 HSNW exhibits a good photothermal-enhanced POD-like activity, resulting in a high bactericidal efficiency against MDR bacteria and meanwhile accelerating the wound healing *in vivo*.

4. Conclusions

In sum up, we developed a novel nanozyme (LNF/Au_3Cu_1 HSNW) exhibiting the enhanced POD-like catalytic activity for smart antibacterial therapy. The as-prepared LNF/Au_3Cu_1 HSNW with the specific design of confined ultrafine bimetallic gold and copper nanoparticles on the self-assembled amyloid-like nanofibrous network facilitates the H_2O_2 adsorption and reduces the energy barrier for activating the H_2O_2 decomposition to form •OH, displaying the significantly enhanced POD-like activity under the NIR irradiation. As the candidate for smart antibacterial therapy, it exhibits the advantages of highly efficient catalytic reaction to decompose the much lower amount of H_2O_2 (~100 μM) to form •OH for bacterial attacking under NIR. Combined with capturing microbial pathogens by the fibrous networks and synergistic effects of the enhanced •OH attacking and the photothermal ablation by LNF/Au_3Cu_1 HSNW, it results in a high bactericidal efficiency against MDR bacteria and the accelerated wound healing *in vivo*. The strategy we proposed in this work could show three advantages, 1) as a template on confining and aligning ultrasmall bimetallic NPs on the lysozyme amyloid-like nanofibrous networks with the simple reduction, 2) the collection and alignment of bimetallic NPs on the fibrils in a controlled manner improving the NIR absorption for accelerating the catalytic reaction rate, 3) the supramolecular fibrous networks effectively capturing the bacteria and allowing the catalytic attack around the bacterial surfaces, which will shed light on the design of novel nanozyme for smart antibacterial therapy, and the variety of other biomedical applications.

Author contribution stament

Yonghai Feng, Conceptualization Lead; Formal analysis Lead; Investigation Methodology Lead; Writing–review & editing Lead, **Zerui Cheng**, Conceptualization Lead; Project administration Lead; Writing-review & editing Equal, **Anne-Kathrine Kure Larsen**, Software Lead; Methodology Supporting; Supervision Supporting, **Hui Shi**, Methodology Equal; Supervision Supporting, **Tongtong Sun**, Visualization Equal; Writing-review & editing Supporting, **Peng Zhang**, Conceptualization

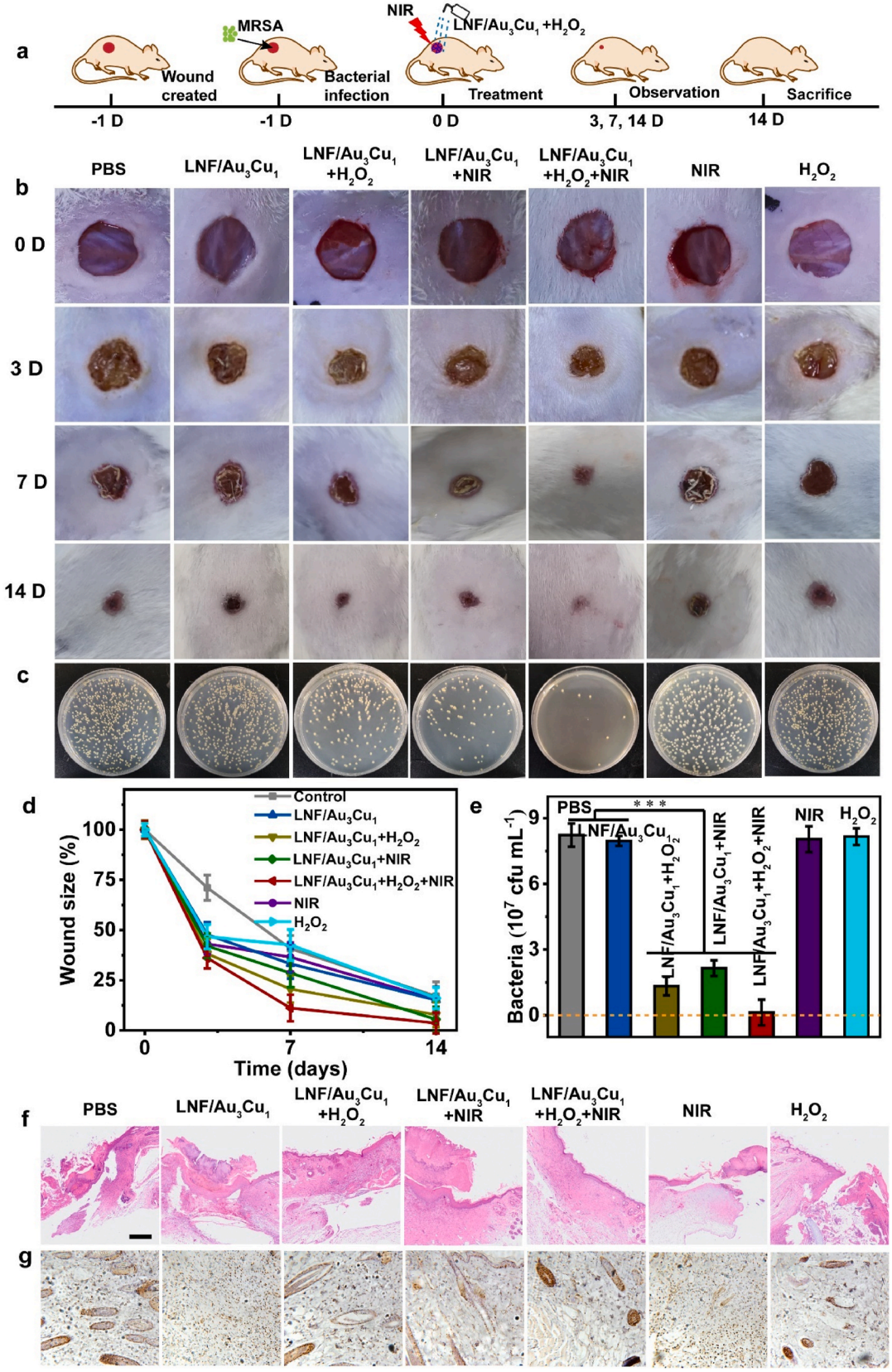

Fig. 4. Disinfection and wound healing of mouse with the different treatments. (a) Schematic diagram of treatment strategy in the MRSA infected mouse wound model. (b) Photographs of infective wounds with different treatments from Day 0 to Day 14. (c) Bacteria separated from different wound tissue were cultured on agar plates according to the different treatments. (d) Quantitative measurement of the wound size over 14 days. (e) Number of bacteria surviving in the wound tissue of each sample. Data were expressed as mean ± SDs (n = 3). *$p < 0.05$, ***$p < 0.001$. (f) HE and (g) immunohistochemical staining of the wound tissues of wound sections with the treatment after 14 days. The scale bar is 50 μm.

Supporting; Data curation Supporting; Formal analysis Equal, **Mingdong Dong***, Software Equal; Project administration Equal; Resources Supporting; Funding acquisition Supporting, **Lei Liu***, Data curation Equal; Supervision Validation Lead; Writing-review & editing Equal; Funding acquisition Lead.

Declaration of competing interest

The authors declare that they have no known competing financial interests or personal relationships that could have appeared to influence the work reported in this paper.

Data availability

No data was used for the research described in the article.

Acknowledgements

We acknowledge the financial support from the National Natural Science Foundation of China (22072060 and 82160421). Natural Science Foundation of Jiangsu Province (BK20211322).

Appendix A. Supplementary data

Supplementary data to this article can be found online at https://doi.org/10.1016/j.mtbio.2023.100730.

References

[1] D.N. Wilson, Ribosome-targeting antibiotics and mechanisms of bacterial resistance, Nat. Rev. Microbiol. 12 (1) (2014) 35–48.
[2] L. Wang, F. Gao, A. Wang, X. Chen, H. Li, X. Zhang, H. Zheng, R. Ji, B. Li, X. Yu, J. Liu, Z. Gu, F. Chen, C. Chen, Defect-rich adhesive molybdenum disulfide/rGO vertical heterostructures with enhanced nanozyme activity for smart bacterial killing application, Adv. Mater. 32 (48) (2020), 2005423.
[3] H. Wei, L. Gao, K. Fan, J. Liu, J. He, X. Qu, S. Dong, E. Wang, X. Yan, Nanozymes, A clear definition with fuzzy edges, Nano Today 40 (2021), 101269.
[4] R. Zhang, X. Yan, K. Fan, Nanozymes inspired by natural enzymes, Acc. Mater. Res. 2 (7) (2021) 534–547.
[5] Z. Wang, Y. Zhao, Y. Hou, G. Tang, R. Zhang, Y. Yang, X. Yan, K. Fan, A thrombin-activated peptide-templated nanozyme for remedying ischemic stroke via thrombolytic and neuroprotective actions, Adv. Mater. (2023), 2210144.
[6] G. Tang, J. He, J. Liu, X. Yan, K. Fan, Nanozyme for tumor therapy: surface modification matters, Explorations 1 (1) (2021) 75–89.
[7] W. Gao, J. He, L. Chen, X. Meng, Y. Ma, L. Cheng, K. Tu, X. Gao, C. Liu, M. Zhang, K. Fan, D.-W. Pang, X. Yan, Deciphering the catalytic mechanism of superoxide dismutase activity of carbon dot nanozyme, Nat. Commun. 14 (1) (2023) 160.
[8] M. Mirhosseini, A. Shekari-Far, F. Hakimian, B.F. Haghiralsadat, S.K. Fatemi, F. Dashtestani, Core-shell Au@Co-Fe hybrid nanoparticles as peroxidase mimetic nanozyme for antibacterial application, Process Biochem. 95 (2020) 131–138.
[9] W.-C. Hu, M.R. Younis, Y. Zhou, C. Wang, X.-H. Xia, In situ fabrication of ultrasmall gold nanoparticles/2D MOFs hybrid as nanozyme for antibacterial therapy, Small 16 (23) (2020), 2000553.
[10] Z. Wang, K. Dong, Z. Liu, Y. Zhang, Z. Chen, H. Sun, J. Ren, X. Qu, Activation of biologically relevant levels of reactive oxygen species by Au/g-C_3N_4 hybrid nanozyme for bacteria killing and wound disinfection, Biomaterials 113 (2017) 145–157.
[11] X. Liao, Q. Xu, H. Sun, W. Liu, Y. Chen, X.-H. Xia, C. Wang, Plasmonic nanozymes: localized surface plasmonic resonance regulates reaction kinetics and antibacterial performance, J. Phys. Chem. Lett. 13 (1) (2022) 312–323.
[12] Y. Zhong, T. Wang, Z. Lao, M. Lu, S. Liang, X. Cui, Q.-l. Li, S. Zhao, Au-Au/IrO_2@Cu(PABA) reactor with tandem enzyme-mimicking catalytic activity for organic dye degradation and antibacterial application, ACS Appl. Mater. Interfaces 13 (18) (2021) 21680–21692.
[13] Q. Mu, Y. Sun, A. Guo, X. Xu, B. Qin, A. Cai, A bifunctionalized $NiCo_2O_4$-Au composite: intrinsic peroxidase and oxidase catalytic activities for killing bacteria and disinfecting wound, J. Hazard Mater. 402 (2021), 123939.
[14] Q. Xu, X. Liao, W. Hu, W. Liu, C. Wang, Plasmon induced dual excited synergistic effect in Au/metal–organic frameworks composite for enhanced antibacterial therapy, J. Mater. Chem. B 9 (46) (2021) 9606–9614.
[15] L. Yan, J. Mu, P. Ma, Q. Li, P. Yin, X. Liu, Y. Cai, H. Yu, J. Liu, G. Wang, A. Liu, Gold nanoplates with superb photothermal efficiency and peroxidase-like activity for rapid and synergistic antibacterial therapy, Chem. Commun. 57 (9) (2021) 1133–1136.
[16] Y. Tao, E. Ju, J. Ren, X. Qu, Bifunctionalized mesoporous silica-supported gold nanoparticles: intrinsic oxidase and peroxidase catalytic activities for antibacterial applications, Adv. Mater. 27 (6) (2015) 1097–1104.
[17] J. Shan, K. Yang, W. Xiu, Q. Qiu, S. Dai, L. Yuwen, L. Weng, Z. Teng, L. Wang, Cu_2MoS_4 nanozyme with NIR-II light enhanced catalytic activity for efficient eradication of multidrug-resistant bacteria, Small 16 (40) (2020), 2001099.
[18] K. Yang, W. Xiu, Y. Li, D. Wang, Q. Wen, L. Yuwen, X. Li, Z. Yin, B. Liang, L. Wang, NIR-responsive MoS_2–Cu_2WS_4 nanosheets for catalytic/photothermal therapy of methicillin-resistant Staphylococcus aureus infections, Nanoscale 14 (27) (2022) 9796–9805.
[19] J. Bai, Y. Feng, W. Li, Z. Cheng, J.M. Rosenholmc, H. Yang, G. Pan, H. Zhang, D. Geng, Alternative copper-based single-atom nanozyme with superior multienzyme activities and nir-ii responsiveness to fight against deep tissue infections, Research 6 (2023), 0031.
[20] Y. Feng, F. Chen, J.M. Rosenholm, L. Liu, H. Zhang, Efficient nanozyme engineering for antibacterial therapy, Mater. Futures 1 (2) (2022), 023502.
[21] S. Hatz, J.D.C. Lambert, P.R. Ogilby, Measuring the lifetime of singlet oxygen in a single cell: addressing the issue of cell viability, Photoch. Photobio.Sci. 6 (10) (2007) 1106–1116.
[22] Y. Sang, W. Li, H. Liu, L. Zhang, H. Wang, Z. Liu, J. Ren, X. Qu, Construction of nanozyme-hydrogel for enhanced capture and elimination of bacteria, Adv. Funct. Mater. 29 (22) (2019), 1900518.
[23] F. Cao, L. Zhang, H. Wang, Y. You, Y. Wang, N. Gao, J. Ren, X. Qu, Defect-rich adhesive nanozymes as efficient antibiotics for enhanced bacterial inhibition, Angew. Chem. Int. Ed. 58 (45) (2019) 16236–16242.
[24] Z. Liu, X. Zhao, B. Yu, N. Zhao, C. Zhang, F.-J. Xu, Rough carbon–iron oxide nanohybrids for near-infrared-II light-responsive synergistic antibacterial therapy, ACS Nano 15 (4) (2021) 7482–7490.
[25] F. Wei, X. Cui, Z. Wang, C. Dong, J. Li, X. Han, Recoverable peroxidase-like Fe3O4@MoS2-Ag nanozyme with enhanced antibacterial ability, Chem. Eng. J. 408 (2021), 127240.
[26] L. Zhang, Z. Liu, Q. Deng, Y. Sang, K. Dong, J. Ren, X. Qu, Nature-inspired construction of MOF@COF nanozyme with active sites in tailored microenvironment and pseudopodia-like surface for enhanced bacterial inhibition, Angew. Chem. Int. Ed. 60 (7) (2021) 3469–3474.
[27] S. Lu, X. Li, J. Zhang, C. Peng, M. Shen, X. Shi, Dendrimer-stabilized gold nanoflowers embedded with ultrasmall iron oxide nanoparticles for multimode imaging–guided combination therapy of tumors, Adv. Sci. 5 (12) (2018), 1801612.
[28] Y. Feng, Q. Chen, Q. Yin, G. Pan, Z. Tu, L. Liu, Reduced graphene oxide functionalized with gold nanostar nanocomposites for synergistically killing bacteria through intrinsic antimicrobial activity and photothermal ablation, ACS Appl. Bio Mater. 2 (2) (2019) 747–756.
[29] P. Chairatana, E.M. Nolan, Molecular basis for self-assembly of a human host-defense peptide that entraps bacterial pathogens, J. Am. Chem. Soc. 136 (38) (2014) 13267–13276.
[30] Y. Feng, H. Wang, J. Zhang, Y. Song, M. Meng, J. Mi, H. Yin, L. Liu, Bioinspired synthesis of Au nanostructures templated from Amyloid β peptide assembly with enhanced catalytic activity, Biomacromolecules 19 (7) (2018) 2432–2442.
[31] H. Gui, Y. Feng, L. Qiang, T. Sun, L. Liu, Core/shell structural ultra-small gold and amyloid peptide nanocomposites with effective bacterial surface adherence and enhanced antibacterial photothermal ablation, Smart Mater. Med. 2 (2021) 46–55.
[32] T. Sun, Y. Feng, J. Peng, Y. Hao, L. Zhang, L. Liu, Cofactors-like peptide self-assembly exhibiting the enhanced catalytic activity in the peptide-metal nanocatalysts, J. Colloid Interface Sci. 617 (2022) 511–524.
[33] P. Lv, L. Qiu, C. Zhao, G. Fang, J. Liu, S. Wang, Synthesis of fluorescent Au clusters using self-assembled tripeptides as reducing soft templates, ChemNanoMat 5 (2) (2019) 158–162.
[34] K. Loza, M. Heggen, M. Epple, Synthesis, Structure, Properties, and applications of bimetallic nanoparticles of noble metals, Adv. Funct. Mater. 30 (21) (2020), 1909260.
[35] M. Kuhn, T.K. Sham, Charge redistribution and electronic behavior in a series of Au-Cu alloys, Phys. Rev. B 49 (3) (1994) 1647–1661.
[36] I. Platzman, R. Brener, H. Haick, R. Tannenbaum, Oxidation of polycrystalline copper thin films at ambient conditions, J. Phys. Chem. C 112 (4) (2008) 1101–1108.
[37] K. Uvdal, P. Bodö, B. Liedberg, l-cysteine adsorbed on gold and copper: an X-ray photoelectron spectroscopy study, J. Colloid Interface Sci. 149 (1) (1992) 162–173.
[38] W. Zhan, J. Wang, H. Wang, J. Zhang, X. Liu, P. Zhang, M. Chi, Y. Guo, Y. Guo, G. Lu, S. Sun, S. Dai, H. Zhu, Crystal structural effect of AuCu alloy nanoparticles on catalytic CO oxidation, J. Am. Chem. Soc. 139 (26) (2017) 8846–8854.
[39] A. Dahiya, M. Verma, P.S. Kumar, Plasmonic applications of gold-copper bimetallic alloy nanoparticles, Plasmonics 17 (5) (2022) 2173–2186.
[40] L. Jiao, J. Wu, H. Zhong, Y. Zhang, W. Xu, Y. Wu, Y. Chen, H. Yan, Q. Zhang, W. Gu, L. Gu, S.P. Beckman, L. Huang, C. Zhu, Densely isolated FeN_4 sites for peroxidase mimicking, ACS Catal. 10 (11) (2020) 6422–6429.
[41] W. Yin, J. Yu, F. Lv, L. Yan, L.R. Zheng, Z. Gu, Y. Zhao, Functionalized nano-MoS_2 with peroxidase catalytic and near-infrared photothermal activities for safe and synergetic wound antibacterial applications, ACS Nano 10 (12) (2016) 11000–11011.